

University of Wollongong

Research Online

Faculty of Engineering and Information
Sciences - Papers: Part B

Faculty of Engineering and Information
Sciences

2018

Locomotion analysis and optimization of actinomorphic robots with soft arms actuated by shape memory alloy wires

Chunshan Liu

University of Science and Technology of China

Erbao Dong

University of Science and Technology of China

Min Xu

University of Science and Technology of China, xumin@ustc.edu.cn

Gursel Alici

University of Wollongong, gursel@uow.edu.au

Jie Yang

University of Science and Technology of China

Follow this and additional works at: <https://ro.uow.edu.au/eispapers1>



Part of the [Engineering Commons](#), and the [Science and Technology Studies Commons](#)

Recommended Citation

Liu, Chunshan; Dong, Erbao; Xu, Min; Alici, Gursel; and Yang, Jie, "Locomotion analysis and optimization of actinomorphic robots with soft arms actuated by shape memory alloy wires" (2018). *Faculty of Engineering and Information Sciences - Papers: Part B*. 1775.

<https://ro.uow.edu.au/eispapers1/1775>

Research Online is the open access institutional repository for the University of Wollongong. For further information contact the UOW Library: research-pubs@uow.edu.au

Locomotion analysis and optimization of actinomorphic robots with soft arms actuated by shape memory alloy wires

Abstract

This article presents the locomotion analysis and optimization of actinomorphic soft robots, which are composed of soft arms actuated by shape memory alloy wires. The soft arm that is a composite modular structure is actuated by a self-sensing feedback control strategy. A theoretical model was established to describe the deformation of the soft arm, combining the Euler-Bernoulli beam model of the soft arm with the constitutive model and the heat transfer model of the shape memory alloy wire. The kinematics of the actinomorphic soft robot was analyzed using the modified Denavit-Hartenberg method, and the motion equation of the actinomorphic soft robot was presented based on the quasi-static hypothesis. Results show that the actinomorphic soft robot moves with a zig-zag pattern. The locomotion of four actinomorphic soft robots with three to six arms was analyzed, and the gait parameters of each locomotion type were optimized. The optimization results indicate that the three-arm actinomorphic robot with certain gait parameters has the best performance and achieves a maximum stride length of 75 mm. A series of experiments were conducted to investigate the movement performance of the three-arm actinomorphic robot in various environments.

Disciplines

Engineering | Science and Technology Studies

Publication Details

Liu, C., Dong, E., Xu, M., Alici, G. & Yang, J. (2018). Locomotion analysis and optimization of actinomorphic robots with soft arms actuated by shape memory alloy wires. *International Journal of Advanced Robotic Systems*, 15 (4), 1-14.

Locomotion analysis and optimization of actinomorphic robots with soft arms actuated by shape memory alloy wires

Chunshan Liu¹, Erbao Dong¹, Min Xu¹, Gursel Alici²  and Jie Yang¹

Abstract

This article presents the locomotion analysis and optimization of actinomorphic soft robots, which are composed of soft arms actuated by shape memory alloy wires. The soft arm that is a composite modular structure is actuated by a self-sensing feedback control strategy. A theoretical model was established to describe the deformation of the soft arm, combining the Euler–Bernoulli beam model of the soft arm with the constitutive model and the heat transfer model of the shape memory alloy wire. The kinematics of the actinomorphic soft robot was analyzed using the modified Denavit–Hartenberg method, and the motion equation of the actinomorphic soft robot was presented based on the quasi-static hypothesis. Results show that the actinomorphic soft robot moves with a zig-zag pattern. The locomotion of four actinomorphic soft robots with three to six arms was analyzed, and the gait parameters of each locomotion type were optimized. The optimization results indicate that the three-arm actinomorphic robot with certain gait parameters has the best performance and achieves a maximum stride length of 75 mm. A series of experiments were conducted to investigate the movement performance of the three-arm actinomorphic robot in various environments.

Keywords

Soft robot, locomotion analysis, gait optimization, bio-inspiration, shape memory alloy

Date received: 25 July 2017; accepted: 30 May 2018

Topic: Bioinspired Robotics

Topic Editor: Mohsen Shahinpoor

Associate Editor: Claudio Rossi

Introduction

Currently, robots are employed in an extensive range of applications from manufacturing to domestic service. Conventional, rigid-bodied robots are typically composed of rigid links and joints, and they could perform tasks that require speed and precision in manufacturing. But rigid-bodied robots often lack compliance and are unsafe for human-centered tasks. Soft robots, primarily composed of soft materials, provide an alternative to bridge the gap between humans and machines.¹ Soft robots have a continuous deformable structure and result in conforming to unknown objects and conditions. Soft robots are attracting the attention of many researchers due to their promising applications and satisfactory performance.^{2–5}

The actuation is one of the key issues for soft-robotic systems. Various actuators have been used to develop soft robots such as pneumatic actuation, dielectric elastomer

¹ Department of Precision Machinery and Precision Instrumentation, University of Science and Technology of China, Anhui, People's Republic of China

² School of Mechanical, Materials and Mechatronic Engineering, and ARC Centre of Excellence for Electromaterials, University of Wollongong, New South Wales, Australia

Corresponding author:

Erbao Dong, Department of Precision Machinery and Precision Instrumentation, University of Science and Technology of China, Hefei, Anhui 230026, People's Republic of China.

Email: ebdong@ustc.edu.cn



Creative Commons CC BY: This article is distributed under the terms of the Creative Commons Attribution 4.0 License

(<http://www.creativecommons.org/licenses/by/4.0/>) which permits any use, reproduction and distribution of the work without further permission provided the original work is attributed as specified on the SAGE and Open Access pages (<https://us.sagepub.com/en-us/nam/open-access-at-sage>).

actuators (DEAs), ionic polymer metal composite (IPMC), electroactive polymer actuators, and shape memory alloy (SMA) wires or springs.^{6–9} A pneumatically actuated robot fabricated by soft lithography has been demonstrated to navigate obstacles by combining a crawling gait with undulation gaits.¹⁰ Soft grippers based on DEAs have been designed to manipulate deformable, fragile objects of any shape.¹¹ A pectoral-fin-mimicking manta ray consisting of a polydimethylsiloxane (PDMS) membrane using four IPMCs has been developed to achieve the undulating locomotion.¹² A robotic insect inspired by a flea has been built to achieve jumping on water using planar SMA actuators.¹³ Compared with other types of actuators, SMAs cannot only offer a high power-to-weight ratio and miniaturize the mechanism but also generate explosive force. In addition, SMAs have diverse crystal structures under different phases (such as the martensite phase and austenite phase),¹⁴ suggesting that the electrical and mechanical properties of SMAs vary with their phase transformation. Based on these properties, SMAs can achieve self-sensing feedback control,^{15–18} where SMAs can act as both an actuator and a sensor. Therefore, SMAs are suitable for engineering and technical applications in various fields.^{19–22}

Recently, many soft robots have been designed for different functions. Some robots may serve as manipulators and complete grasping tasks, such as a simple gripper,²³ a soft robot arm,²⁴ and a soft hand,²⁵ whereas others may achieve good locomotion, such as walking, rolling, jumping, and swimming. A pneumatically actuated, quadrupedal soft robot has been fabricated to achieve walking gait in a variety of adverse environmental conditions.²⁶ A caterpillar-inspired soft robot can generate rolling locomotion using SMA coils.²⁷ A tripod soft robot has been demonstrated to achieve jumping locomotion using a chemical reaction.²⁸ An octopus-inspired, multi-modal, soft robot can perform shape-changing pulsed-jet propulsion and benthic legged-locomotion based on a hybrid least squares/genetic algorithm-based method.²⁹ These soft robots own good locomotive performance and show potential for many potential applications (such as environmental monitoring or search and rescue operations).

Many soft robots, which show good performance, are inspired by biological systems. For example, a fluidic elastomer robotic snake has been developed to synthesize the interesting locomotion gait of snakes.³⁰ An inchworm-inspired robot has been designed to achieve both two-way linear and turning movement.³¹ A turtle mimetic soft robot driven by flipper actuators has been proposed to produce distinct motions corresponding to different swimming gaits.³² A miniature jellyfish-inspired robot can achieve a diversity of propulsion modes using jet propulsion.³³ In the biological locomotion field, symmetry is one of the typical features, such as the bilateria and the radiata. Among these creatures, the radiata (e.g. brittle star and starfish) achieves a high mobility for the radial symmetry of its body. As the shape of the radiata is actinomorphic, its gait pattern can be

easily modularized. However, a few studies have been conducted on the locomotion of the actinomorphic soft robot. A starfish-like soft robot has been developed to achieve multigait movements.³⁴ However, it moves slowly in various terrains. A soft robot inspired from the starfish has been designed to achieve various locomotions.³⁵ However, the locomotion mechanism of the soft robot is not analyzed.

This article investigates the locomotion of the actinomorphic soft robot composed of soft arms and the effect of gait parameters on the locomotive performance of the actinomorphic soft robot. First, actinomorphic soft robots with different number of soft arms were designed with a layer casting technique, and a self-sensing feedback control strategy was adopted to modulate the bending range of the soft arm. Then, theoretical models were established including the model of the soft arm and the kinematics as well as the motion equation of the actinomorphic soft robot, to analyze the motion of the actinomorphic soft robot. Furthermore, each locomotion type corresponding to each actinomorphic soft robot with a specific number of arms was presented, and relative gait parameters were optimized to select the one with the best performance. In addition, a series of experiments were conducted on a three-arm actinomorphic soft robot to investigate its basic movements and performance in various environments.

System design of actinomorphic soft robots

Design and fabrication of actinomorphic robots

Actinomorphic soft robots with three to six arms were designed as shown in Figure 1. Each actinomorphic soft robot is primarily comprised of two parts: soft arms and a regular polygon rack. The soft arm was fabricated by a molding technique and a layer casting technique.³⁶ Their soft bodies were manufactured using PDMS (Sylgard 184, Dow Corning [Shepherdsville, Kentucky, United States]), and a thin polyvinyl chloride (PVC) polymer plate was embedded in PDMS. These soft robots were actuated by SMA wires (diameter of 0.15 mm, a transition temperature of 90°C; Flexinol[®] nickel–titanium alloy wires by Dynalloy, Inc., Irvine, California, USA). Multiple SMA wires can be connected in a parallel or serial system.³⁷ It could increase the force capabilities of the SMA actuator to connect SMA wires mechanically in parallel.³⁸ However, the power supply requirement may be affected by such an arrangement. Besides, this arrangement has a negative effect on the motion of the actinomorphic soft robot for the wires at the end of the actuator. Therefore, SMA wires were arranged in M-shaped layouts with a serial manner. Racks were fabricated via three-dimensional (3D) printing technology with acrylonitrile butadiene styrene plastic in the form of regular polygons. Table 1 lists the sizes and masses of these soft robots.

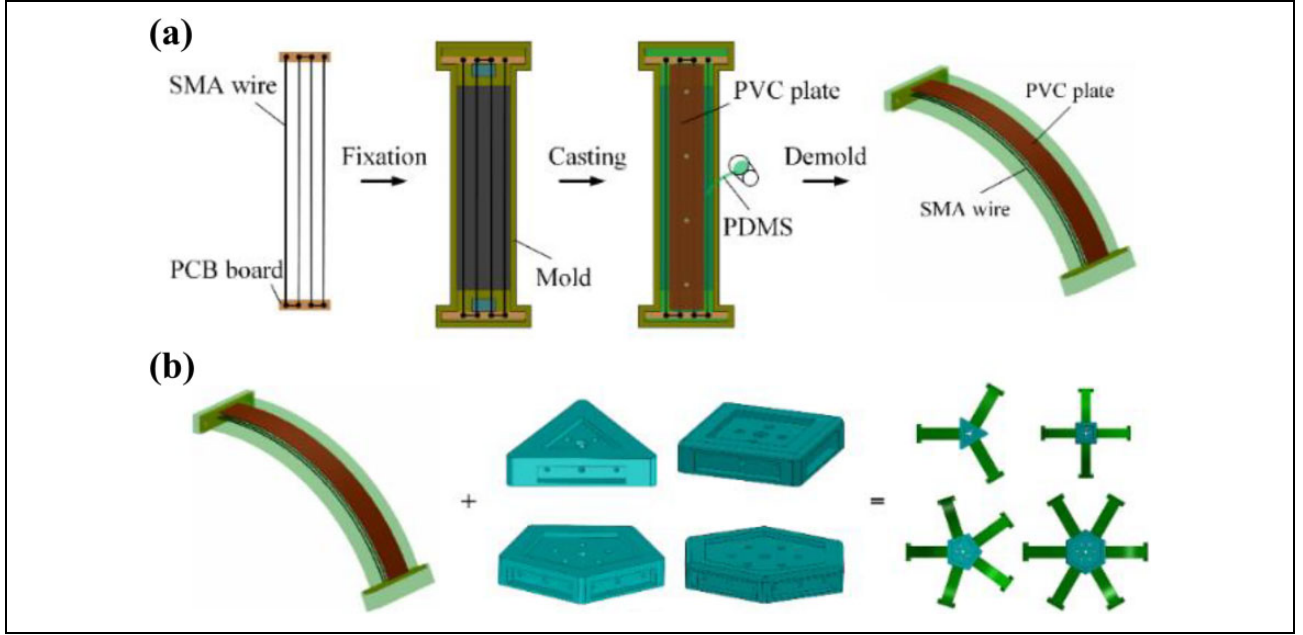


Figure 1. Structures of actinomorphic soft robots. (a) Fabrication of the soft arm. (b) Actinomorphic soft robots with multiple arms.

Table 1. Body sizes and masses of actinomorphic soft robots.

Number of arms	Height (mm)	Length (mm)	Mass (g)
3	43	176	36
4	43	184	47
5	43	192	59
6	43	200	72

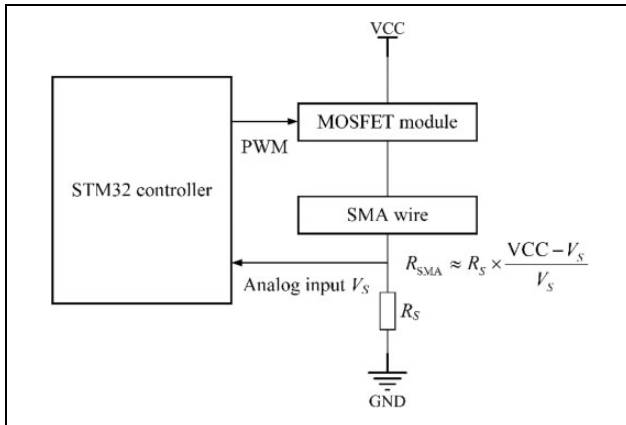


Figure 2. Circuit schematic of the self-sensing feedback control strategy.

Actuation strategy of the soft arm

Figure 2 shows a circuit diagram of the self-sensing feedback control strategy for actuating the soft arm. An STM32F103 processor was employed to send the control signal via the PWM output and measure the voltage V_S via the analogue input. A MOSFET IRF540 module, acted as the switching element, was used to control the heating or cooling state of the

SMA wire. A precise resistor R_S was connected in series to the SMA wire to indirectly measure the resistance of the SMA wire during the actuation process. The effect of the MOSFET on the circuit can be neglected when the on-resistance of the MOSFET is low. A direct current (DC) voltage source (model GPR-3060D) was used to supply a DC voltage for the SMA wire. In the following experiments, the input of the SMA wire is described by the supply current that is equal to the supply voltage VCC divided by the initial resistance.

Actinomorphic soft robots follow a wave gait while moving according to the sequential diagrams, in which each arm has two processes: a heating and a cooling process. In the heating process, a rapid fluctuation occurs in the SMA resistance when the SMA wire of the soft arm undergoes a phase transformation. Therefore, the deformation of each arm can be regulated. The set duty cycle is high during heating and low during cooling. The switch controller shown in Figure 3 can switch between these two processes according to the sequential diagrams. Here, the high duty cycle was set to 100%, and the low duty cycle was set to 0.

In the heating process, the SMA resistance exhibits a regular variation when the soft arm is under a nonloaded condition, as shown in Figure 4(a). Within the ranges of A–B and C–D, the SMA resistance is primarily affected by temperature. Within the range of B–C, the SMA resistance decreases monotonously because of the occurrence of phase transformation dominating the change of the SMA resistance. A normalized resistance λ is utilized between the maximal resistance and the minimal resistance, as shown in Figure 4(a). Figure 4(b) shows the bending range of the soft arm from B–C, which is the angle between the final and initial bending angle. The bending angle β is used to quantify the bending range δ . According to Figure 4(b), the bending range of the

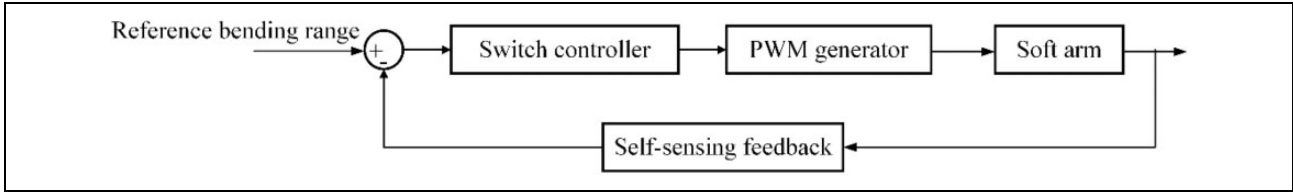


Figure 3. Control block diagram of one arm for walking.

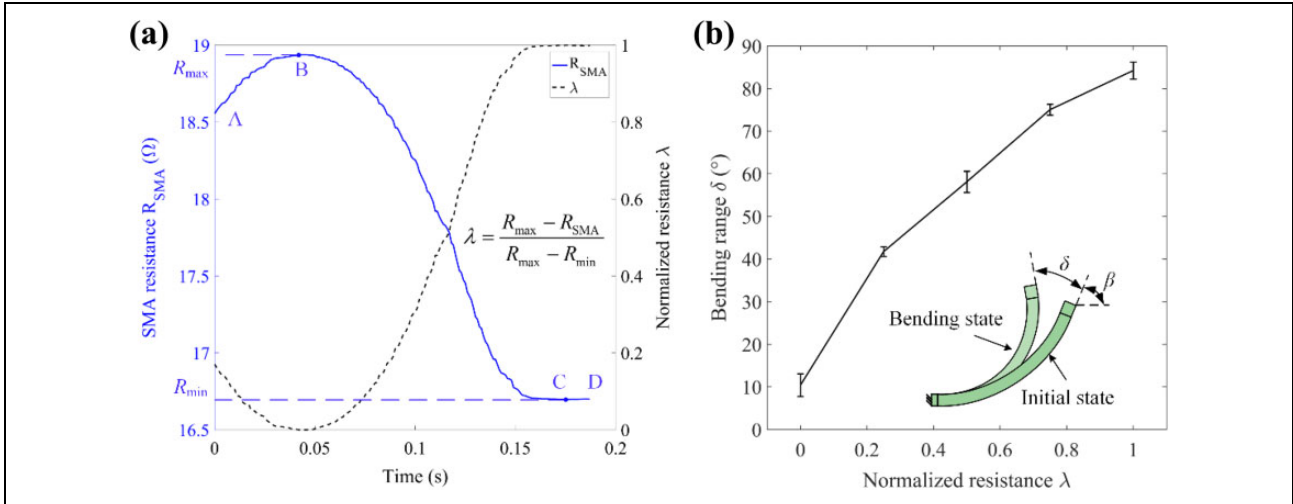


Figure 4. Properties of the soft arm under idling (supply current = 1.54 A, $R_S = 1 \Omega$, at room temperature of 27°C). (a) The resistance and normalized resistance of the SMA wire versus time in the heating process. (b) Bending range of the soft arm versus the normalized resistance of the SMA wire in range B–C. SMA: shape memory alloy.

soft arm is in an approximate linear correlation with the normalized resistance. Based on these properties, the self-sensing feedback control strategy was adopted to control the soft arm. The bending range of the soft arm was modulated by limiting the analogue input $V_S(\lambda)$. $V_S(\lambda)$, which can be directly measured, decreases monotonically with the SMA resistance

$$V_S(\lambda) = \frac{R_S + R_{\max}}{R_S + R_{SMA}(\lambda)} V_{\min} \quad (1)$$

where V_{\min} is the minimum value of the voltage V_S across the precise resistor in the experiment, and $R_{SMA}(\lambda)$ can be obtained using

$$R_{SMA}(\lambda) = R_{\max} - \lambda(R_{\max} - R_{\min}) \quad (2)$$

The analogue input $V_S(\lambda)$ was applied as a threshold value to modify the duty cycle, and therefore, the bending range could be regulated. In addition, the overheating of the SMA wire could be prevented with the self-sensing feedback control strategy.

Locomotion analysis of the actinomorphic soft robot

Model of the soft arm

Many researchers have conducted studies of the bending actuator embedded with SMA wires.³⁹ Taking geometric

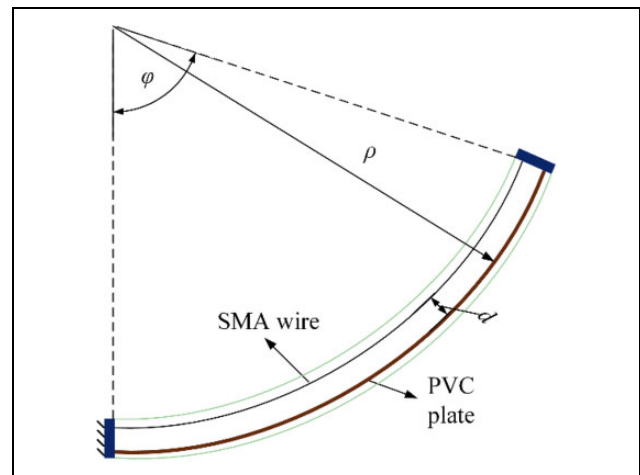


Figure 5. Schematic of the soft arm after actuation.

nonlinearity of the actuator and hysteretic nonlinearity of the SMA wire into account, the model of the bending actuator is established.⁴⁰ A dynamic model of the actuator associated with the constitutive characteristic of the SMA wire is built.⁴¹ A model based on the constitutive model of the SMA wire is established.⁴² However, they neglect the latent heat of transformation. Here, a model is developed to obtain the bending capability of the soft arm. Figure 5 shows a schematic of the soft arm deformed by a

Table 2. Parameters in the model of the soft arm.

Description (parameter)	Value (unit)
Initial size of the soft arm (length \times width \times high)	80 \times 20 \times 5 mm
Distance between the SMA wire and PVC surface (d)	1.7 mm
SMA wire diameter (d_{SMA})	0.15 mm
Length of the SMA wire (l_{SMA})	320 mm
Resistance per length (μ)	55 Ω/m
Density (ρ_{SMA})	6.45 g/cm ³
Specific heat capacity (c_{SMA})	837 J/(kg \times $^{\circ}C$)
Latent heat of transformation (H)	24.2 $\times 10^3$ J/kg
Austenite start temperature (A_s)	80 $^{\circ}C$
Austenite finish temperature (A_f)	108 $^{\circ}C$
Martensitic start temperature (M_s)	78 $^{\circ}C$
Martensitic finish temperature (M_f)	60 $^{\circ}C$
Austenitic Young's modulus (E_A)	83 GPa
Martensitic Young's modulus (E_M)	28 GPa
Maximum residual strain (ε_L)	6.6%
Effect of stress on austenite temperature (C_A)	12 MPa/ $^{\circ}C$
Effect of stress on martensitic temperature (C_M)	10 MPa/ $^{\circ}C$

SMA: shape memory alloy; PVC: polyvinyl chloride.

contraction force of SMA wire, and the parameters of this soft arm are listed in Table 2. Three assumptions are made in the model: (i) the soft arm behaves as a Euler beam throughout the bending deformation, and its bending shape is approximated as a circular arc; (ii) the PVC surface is the neutral plane of the soft arm, and the distance d between the SMA wire as well as the PVC surface is constant during actuation; and (iii) the temperature variation of the PDMS is negligible if the heating time is short.

When the soft arm is deformed by a bending moment generated by the contraction force F_{SMA} of the SMA wire, with its bending deformation measured by the bending deformation φ , then

$$\frac{F_{SMA}d}{E_{SA}I_{SA}} = \frac{1}{\rho} \quad (3)$$

where E_{SA} is the effective elastic modulus of the soft arm, I_{SA} is the area moment of inertia of the soft arm, and ρ is the radius of curvature of the soft arm. Because the bending shape of the soft arm is approximated as a circular arc, the radius of curvature ρ is given by

$$\rho = \frac{L_{SA}}{\varphi} \quad (4)$$

where L_{SA} is the length of the soft arm. The bending deformation φ can be approximately expressed by

$$\varphi = \frac{(\varepsilon_L - \varepsilon_{SMA})L_{SA}}{d} \quad (5)$$

where ε_{SMA} is the strain of the SMA wire and ε_L is the maximum residual strain of the SMA wire.

According to equations (1) to (3), the contraction force of the SMA wire is

$$F_{SMA} = \frac{E_{SA}I_{SA}}{d^2}(\varepsilon_L - \varepsilon_{SMA}) \quad (6)$$

The equilibrium state of the soft arm is given by

$$F_{SMA} = \sigma_{SMA}A_{SMA} - F_{ini} \quad (7)$$

where σ_{SMA} is the stress in the SMA wire, A_{SMA} is the cross-sectional area of the SMA wire, and F_{ini} is the initial pull force of the SMA wire.

The resulting stress of the SMA wire is

$$\sigma_{SMA} = k(\varepsilon_L - \varepsilon_{SMA}) + \sigma_{ini} \quad (8)$$

where $k = (E_{SA}I_{SA})/(d^2A_{SMA})$ and $\sigma_{ini} = F_{ini}/A_{SMA}$.

When the temperature of the SMA wire is higher than the austenite start temperature A_s , the SMA wire starts to transfer from the martensite to the austenite phase and generates the contraction force. The behavior of the SMA wire is described by Liang–Rogers model⁴³

$$\dot{\sigma}_{SMA} = E(\xi)\dot{\varepsilon}_{SMA} + \Theta\dot{T} + \Omega(\xi)\dot{\xi} \quad (9)$$

where $E(\xi)$ is the Young's modulus of the SMA wire, Θ is the thermoelastic tensor for the SMA wire and is assumed to be negligible, T is the temperature of the SMA wire, $\Omega(\xi)$ is the phase transformation tensor, and ξ is the martensite fraction. $E(\xi)$ is assumed to be linear with the martensite fraction, namely $E(\xi) = E_A + \xi(E_M - E_A)$, where E_A and E_M are Young's moduli when austenite is 100% and martensite is 100%, respectively. $\Omega(\xi)$ is related to $E(\xi)$ and can be defined by $\Omega(\xi) = -\varepsilon_L E(\xi)$. Therefore, the SMA constitutive model can be simplified as

$$\dot{\sigma}_{SMA} = E(\xi)(\dot{\varepsilon}_{SMA} - \varepsilon_L\dot{\xi}) \quad (10)$$

During the transformation process of the SMA wire from the martensite to austenite (M \rightarrow A), its martensite fraction is expressed by

$$\xi = \frac{\xi_M}{2} \cos[a_A(T - A_s) + b_A\sigma_{SMA}] + \frac{\xi_M}{2}, \quad (11)$$

$$A_s + \frac{\sigma_{SMA}}{C_A} \leq T \leq A_f + \frac{\sigma_{SMA}}{C_A}$$

where $a_A = \pi/(A_f - A_s)$ and $b_A = -a_A/C_A$. ξ_M is the initial martensite fraction prior to the beginning of the M \rightarrow A transformation process. C_A is a constant, representing the effect of stress on the austenite temperature of the SMA wire.

During the transformation process of the SMA wire from the austenite to martensite (A \rightarrow M), its martensite fraction is expressed by

$$\xi = \frac{1 - \xi_A}{2} \cos[a_M(T - M_f) + b_M\sigma_{SMA}] + \frac{1 + \xi_A}{2},$$

$$M_f + \frac{\sigma_{SMA}}{C_M} \leq T \leq M_s + \frac{\sigma_{SMA}}{C_M} \quad (12)$$

where $a_M = \pi/(M_s - M_f)$ and $b_M = -a_M/C_M$. ξ_A is the initial martensite fraction prior to the beginning of the

A \rightarrow M transformation process. C_M is a constant, which represents the effect of stress on the martensite temperature of the SMA wire.

Therefore, the derivatives of equations (11) and (12) can be expressed by

$$\dot{\xi} = \eta_T \dot{T} + \eta_\sigma \dot{\sigma} \quad (13)$$

where

$$\eta_T = \begin{cases} -a_A \frac{\xi_M}{2} \sin[a_A(T - A_s) + b_A \sigma_{SMA}] & M \rightarrow A \\ -a_M \frac{1 - \xi_A}{2} \sin[a_M(T - M_f) + b_M \sigma_{SMA}] & A \rightarrow M \end{cases} \quad (14)$$

$$\eta_\sigma = \begin{cases} -b_A \frac{\xi_M}{2} \sin[a_A(T - A_s) + b_A \sigma_{SMA}] & M \rightarrow A \\ -b_M \frac{1 - \xi_A}{2} \sin[a_M(T - M_f) + b_M \sigma_{SMA}] & A \rightarrow M \end{cases} \quad (15)$$

When the SMA wire is heated through current, its thermal model can be expressed by

$$\rho_{SMA} c_{SMA} V_{SMA} \dot{T} = i_{SMA}^2 R_{SMA} - h S_{SMA} (T - T_{amb}) + \rho_{SMA} V_{SMA} H \dot{\xi} \quad (16)$$

where ρ_{SMA} is the density of the SMA wire, c_{SMA} is the specific heat capacity, V_{SMA} is the volume of the SMA wire, i_{SMA} is the supply current, R_{SMA} is the resistance of the SMA wire, h is the heat transfer coefficient, S_{SMA} is the surface area of the SMA wire, T_{amb} is the ambient temperature, and H is the latent heat of transformation of the SMA wire.

During the actuation process of the SMA wire, the following equations are derived from equations (8) to (16)

$$\begin{bmatrix} \dot{\xi} \\ \dot{T} \\ \dot{\xi} \end{bmatrix} = \begin{bmatrix} f(\sigma, T) \\ \frac{i_{SMA}^2 R_{SMA} - h S_{SMA} (T - T_{amb}) + H f(\sigma, T)}{\rho_{SMA} V_{SMA} c_{SMA}} \\ \frac{E(\xi) \varepsilon_L}{E(\xi) + k} f(\sigma, T) \end{bmatrix} \quad (17)$$

where

$$f(\sigma, T) = \frac{\eta_T \frac{i_{SMA}^2 R_{SMA} - h S_{SMA} (T - T_{amb})}{\rho_{SMA} V_{SMA} c_{SMA}}}{1 + \eta_\sigma k \varepsilon_L \frac{E(\xi)}{E(\xi) + k} - \eta_T \frac{H}{c_{SMA}}} \quad (18)$$

Figure 6 shows the bending range of the soft arm under idling, in which the supply voltage is 30 V with 160 ms heating time in one period. According to Figure 6, the cooling process is longer than the heating process and the

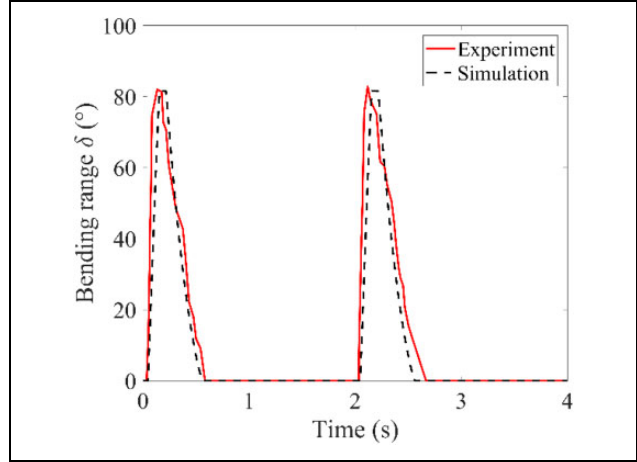


Figure 6. Bending range of the soft arm versus time under idling (heating time = 160 ms, period = 2 s, supply current = 1.54 A).

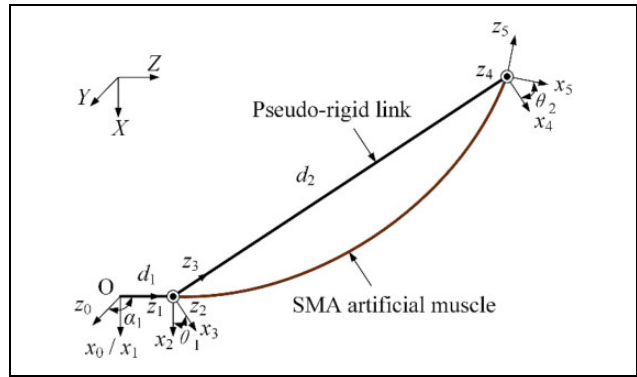


Figure 7. D-H frames for one arm of the actinomorphic soft robot. D-H: Denavit–Hartenberg.

bending range is approximately linear to the time during the heating process. The experimental and simulation results exhibit similar motion, and therefore, the model of the soft arm could be used to analyze the locomotion of the actinomorphic soft robot.

Spatial robot kinematics

To model the kinematics of the actinomorphic soft robot, a modified Denavit–Hartenberg (D-H) method was introduced. The modified D-H method is first proposed to model the kinematics of continuum robots, in which the movement of a planar curve is described by three coupled movements.⁴⁴ To reflect a correct orientation term, the continuum robot section is based on a rigid-link arm consisting of two revolute joints with intersecting axes, followed by a translational and two more revolute joints with intersecting axes in the modified D-H method.⁴⁵

The kinematics of the actinomorphic soft robot is analyzed. The geometric parameters for one arm of the actinomorphic soft robot shown (see Figure 7) are listed

in Table 3. XYZ -system is the world coordinate system, and the actinomorphic soft robot moves in the YZ plane. Frame 0 is located in the geometric center of the 3-D printing rack, in which axis x_0 is parallel to axis X . α_1 is the angle from z_0 -axis to z_1 -axis about x_0 -axis, which is related to the

distribution of the arm. The soft arm is described by a pseudo-rigid link with a coupled link/joint arrangement. Using the D-H table, the homogeneous transformation matrix for the arm can be written as

$${}^0T_5 = \begin{bmatrix} \cos(\theta_1 + \theta_2) & 0 & -\sin(\theta_1 + \theta_2) & -d_2 \sin\theta_1 \\ -\sin\alpha_1 \sin(\theta_1 + \theta_2) & \cos\alpha_1 & -\sin\alpha_1 \cos(\theta_1 + \theta_2) & -\sin\alpha_1(d_1 + d_2 \cos\theta_1) \\ \cos\alpha_1 \sin(\theta_1 + \theta_2) & \sin\alpha_1 & \cos\alpha_1 \cos(\theta_1 + \theta_2) & \cos\alpha_1(d_1 + d_2 \cos\theta_1) \\ 0 & 0 & 0 & 1 \end{bmatrix} \quad (19)$$

where $\theta_2 + \theta_1 = 2\theta_1 = \varphi$.

Locomotion state and motion equation

In the movement of the actinomorphic soft robot, the arm owns two states: swing and supporting state. In the swing state, the arm is off the ground. In the supporting state, the arm could be static or moving depending on the friction force with the ground. The locomotion state is a series of arm states that enable the actinomorphic soft robot to move in the environment. To analyze the locomotion model of the actinomorphic soft robot, an equivalent parallel closed-chain mechanism was proposed, as shown in Figure 8. The ground, the supporting arm, and the 3D printing rack with the swing arm correspond to the frame, link, and end effector of the closed-chain mechanism, respectively. The linkup between the supporting arm and the 3D printing rack is approximate to a revolute pair. The linkups between the ground and the static or moving supporting arm are the revolute pair and cylindrical and planar pair, respectively.

The total degrees of freedom (DOF) in the equivalent closed-chain mechanism is given by

$$\text{DOF} = 6(n + 1) - 5n - \sum_{i=1}^n f_i = n + 6 - \sum_{i=1}^n f_i \quad (20)$$

where n is the number of supporting arms, and $\sum_{i=1}^n f_i$ is the

DOF limited by the linkups between the ground and supporting arms. Because the soft robot could be mobile, the DOF is constrained by

$$1 \leq \text{DOF} \leq 6 \quad (21)$$

If all the supporting arms are moving, then

$$\sum_{i=1}^n f_i = n, \quad \text{DOF} = 6 \quad (22)$$

If there is one static supporting arm, then

$$\sum_{i=1}^n f_i = n + 4, \quad \text{DOF} = 2 \quad (23)$$

If there are two static supporting arms, then

$$\sum_{i=1}^n f_i = n + 8, \quad \text{DOF} < 0 \quad (24)$$

Therefore, during the movement of the actinomorphic soft robot, the locomotion state of the actinomorphic soft robot falls into two categories: all arms are in the moving state and only one arm is the static supporting arm.

During the movement of the actinomorphic soft robot, the bending state of the arm changes with the temperature of the SMA wire, resulting in the variation of the support force and frictional force exerted on the arm. When the state of force equilibrium is broken in the current locomotion state, the soft robot switches from the current locomotion state to the other state in which the equilibrium condition could be satisfied. The switch between locomotion states is related to the state of force equilibrium and input signal of the soft arm.

When the actinomorphic soft robot moves slowly in the environment, its motion is approximated to a quasi-static process. In the quasi-static process, the resultant \mathbf{F} of all forces acting on the soft robot is zero. Therefore, the translational equilibrium and rotational equilibrium equations in the world coordinate system could be expressed by

$$\begin{cases} \sum F_y = 0, & \sum F_z = 0 \\ \sum M_x(\mathbf{F}) = 0 \end{cases} \quad (25)$$

Combined with the model of the soft arm and spatial robot kinematics, the relative position of each arm end relative to the frame 0 could be calculated, and therefore, $2n-3$ distance equations could be derived. The distance equation between two arm ends in the world coordinate system satisfies

$$d(\text{arm}_i, \text{arm}_j) = \|(y_i, z_i) - (y_j, z_j)\| \quad (26)$$

where (y_i, z_i) and (y_j, z_j) are coordinates of arms i and j in the YZ plane, respectively. When all the supporting arms are moving, solutions of these equations could be expressed by

Table 3. D-H table for one arm of the actinomorphic soft robot in Figure 7.

Link i	d_i	θ_i	a_i	α_i
1	0	0	0	α_1
2	d_1	0	0	$-\pi/2$
3	0	θ_1	0	$\pi/2$
4	d_2	0	0	$-\pi/2$
5	0	θ_2	0	$\pi/2$

D-H: Denavit–Hartenberg.

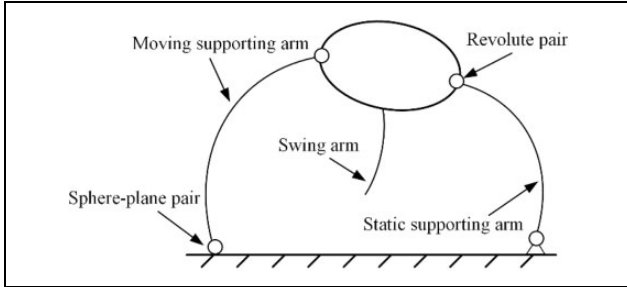


Figure 8. Schematic of an equivalent parallel closed-chain mechanism for an actinomorphic soft robot.

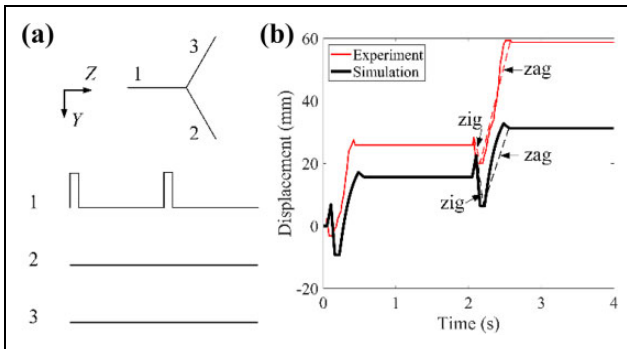


Figure 9. Locomotion of a three-arm soft robot with one actuating arm. (a) Sequential diagram for the locomotion (pulse width = 8%, period = 2 s, supply current = 1.54 A). (b) Displacement–time curve in the Z direction.

$$x = (y_1, z_1, \dots, y_n, z_n)^T \quad (27)$$

When there is one static supporting arm, solutions of these equations could be expressed by

$$x = (y_1, z_1, \dots, y_{k-1}, z_{k-1}, y_{k+1}, z_{k+1}, \dots, y_n, z_n, f_{ky}, f_{kz})^T \quad (28)$$

where k is the index of the static supporting arm, f_{ky} and f_{kz} are the static frictional forces exerted on the arm k .

Figure 9 shows the locomotion of a three-arm soft robot, in which only one arm is actuated. The sequential diagram is shown in Figure 9(a), in which the period is 2 s with the pulse width 160 ms. The displacement of the three-arm soft

robot is shown in Figure 9(b). The experimental and simulation results exhibit similar locomotion characteristics with a zig-zag movement pattern (see Figure 9(b)), due to the switch of the locomotion state caused by the variation of the support force and frictional force. Nevertheless, the stride lengths in one period of the three-arm soft robot in experiment and simulation are different. This is mainly caused by several factors including the quasi-static and pseudo-rigid approximation in the simulation scene and the variable friction coefficient affected by the changing contact surface of the arm in the experiment.

Gait optimization of actinomorphic soft robots

Gait planning for locomotion

Controlling the locomotion of soft robots is challenging because of the difficulty in accurate modeling of the robot–environment interaction. The robot locomotion is formulated as a type of optimization problem,⁴⁶ complex for a multiarm robot such as a six-arm robot, and some of the locomotion is not realistic. Robot locomotion is typically inspired from biology.^{31,32} Inspired by starfish locomotion, two rays are pushed in advance, with three rays behind; or three rays pushed in advance, followed by two rays.⁴⁷ According to this principle, wave gaits were adopted; these actuated the soft robots in a sequential manner with an actuation wave travelling through their bodies from the front toward the rear.

Figure 10 depicts the locomotion of four types of actinomorphic soft robots. These sequential diagrams exhibit a series of wave gaits. Figure 10(a) shows the sequential diagram of a three-arm soft robot. First, arms 2 and 3 are activated and bent, thereby causing the center of gravity to move ahead. Second, arm 1 is activated and bent; this action helps accumulate the elastic potential energy to drive the robot to move forward. Figure 10(b) displays the sequence chart of a four-arm soft robot. First, arm 4 is activated and contracted; the contraction produces forward movement to cause the center of gravity to shift ahead. Second, arms 2 and 3 are activated and bent simultaneously to upraise the body. Third, arm 1 bends and drives the robot crawling motion using the accumulated elastic potential energy. Figure 10(c) shows a five-arm soft robot that moves forward with the wave gait. First, arms 4 and 5 are activated and bent, thereby causing the center of gravity of the body to shift forward. Next, arms 2 and 3 are activated and contracted to hold the entire body. Finally, arm 1 is activated and bent, thereby storing elastic potential energy to cause the entire body to move forward with ground friction. Figure 10(d) shows a six-arm soft robot that achieves forward motion via a series of sequential movements. First, arm 6 is activated and bent, thereby causing the center of gravity of the body to move ahead. Next, arms 4 and 5 are activated and the body raised. Subsequently, arms 2 and 3 are

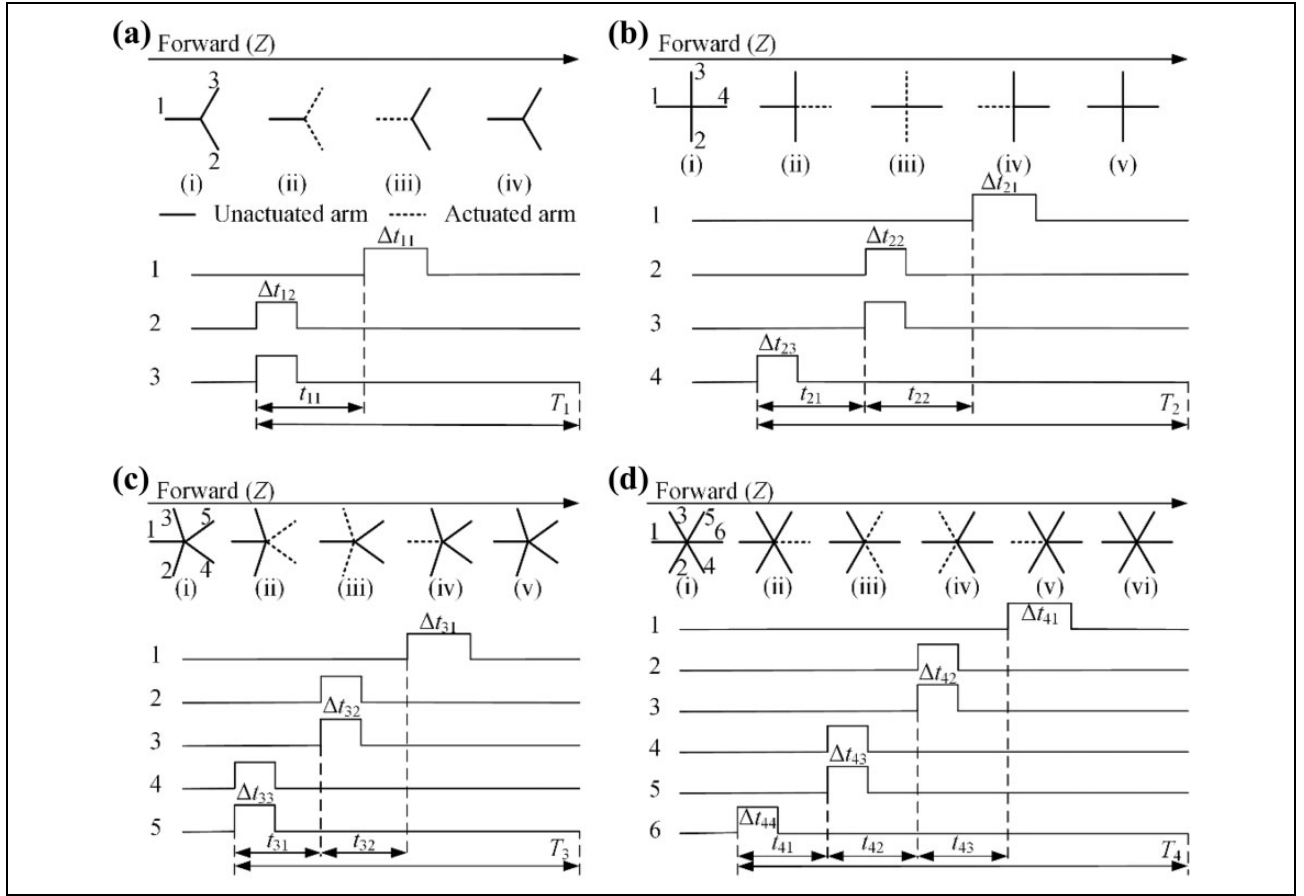


Figure 10. Locomotion of actinomorph soft robots. (a) to (d) are sequential diagrams of the locomotion principle for the three-arm, four-, five-, and six-arm robots, respectively.

activated and contracted to hold the body. Finally, arm 1 is activated and contracted, thereby accumulating elastic potential energy to propel the robot forward. In Figure 10, T_i ($i = 1, 2, 3, 4$) is the period of motion in each locomotion; t_{ij} ($i = 1, 2, 3, 4; j = 1, 2, 3$) is the time interval of the startup time between two adjacent groups of arms in each locomotion; and Δt_{ij} ($i = 1, 2, 3, 4; j = 1, 2, 3, 4$) is the heating time of each arm.

Performance comparisons of the actinomorph soft robots

Four types of actinomorph robot prototypes were designed to investigate the effects of factors, for example, the number of arms and Δt_{ij} , on the performance of the robots. A series of experiments were conducted to select the optimal gait parameters to actuate robots with a satisfactory performance. The heating time Δt_{ij} of each arm was regulated by controlling the corresponding normalized resistance λ_{ij} of each arm according to the self-sensing feedback control strategy, and λ_{ij} corresponds to Δt_{ij} . The period of motion T_i in each locomotion is sufficiently long to prevent the SMA wires from overheating, and these periods were set as 2, 2, 2, and 4 s for three-, four-, five-,

and six-arm robots, respectively. To simplify the experiments, the time intervals t_{ij} were defined to be equivalent in each locomotion, such as $t_{21} = t_{22}$, $t_{31} = t_{32}$, and $t_{41} = t_{42} = t_{43}$, and arm 1 of each robot bent with a maximum bending range, namely, the corresponding normalized resistance λ was set to 1. Several sets of experiments were performed to evaluate the effects of the time interval and heating time on the performance of robots. The time interval t_{ij} ranged from 10 ms to 100 ms with an increment of 30 ms, and the normalized resistance λ_{ij} (which was used to regulate the heating time) ranged from 0.1 to 1.0, with an increment of 0.3. These experiments were conducted on a flat surface at the room temperature of 27°C.

Appendix Tables 1A to 1D list the stride lengths in one period of different robots to accomplish locomotion for the conditions stated in the previous paragraph. According to Appendix Table 1A, the three-arm soft robot could achieve better performance (a longer stride length) when the parameters satisfy the conditions of $0.1 \leq \lambda_{12} \leq 0.4$ or $70 \leq t_{11} \leq 100$. In Appendix Table 1B, the four-arm soft robot could exhibit better performance when $0.1 \leq \lambda_{22} \leq 0.4$ or $70 \leq t_{21} \leq 100$. Appendix Table 1C shows that the five-arm soft robot performs better when $0.4 \leq \lambda_{33} \leq 1.0$ or $0.4 \leq \lambda_{32} \leq 0.7$. As shown in Appendix Table 1D, the

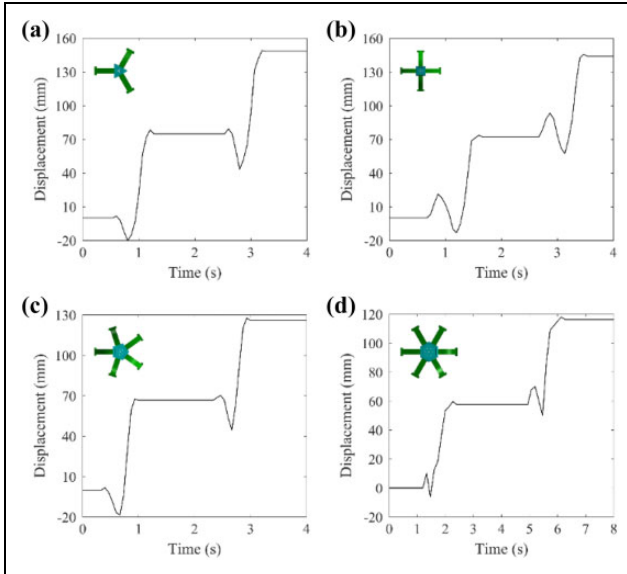


Figure 11. Displacement–time curves of actinomorphic soft robots for forward translation: (a) to (d) are displacement–time curves of the three-, four-, five-, and 6-arm soft robots, respectively.

six-arm soft robot could perform better when $0.4 \leq \lambda_{43} \leq 1.0$ or $40 \leq t_{41} \leq 100$. These results indicate that the gait parameters affect the performance of actinomorphic soft robots with multiple arms.

The maximum periodic stride lengths of the three-, four-, five-, and 6-arm robots are 75, 72, 63, and 58 mm, respectively. Figure 11 shows the displacement–time curves of these robots at the maximum periodic stride lengths, in which the displacements are the trajectories of each center of rack (CoR). These robots exhibit similar locomotion characteristic with a zig-zag movement pattern. Their CoRs move forward for a short distance initially and then backward for a long distance. Afterwards, their CoRs move forward for a long distance and then backward for a short distance. As a result, the CoRs move forward for one stride length. The average stride lengths of the three-, four-, five-, and six-arm robots are 52, 47, 28, and 29 mm, respectively, as shown in Figure 12. The average stride length of the three-arm robot is greater than that of the four-arm robot, and the six-arm robot has a similar average stride length as the five-arm robot. Among these robots, the three-arm robot shows the best performance.

Locomotive performance of the three-arm actinomorphic soft robot

In the natural environment, actinomorphic animals inhabit a wide range of surroundings, for example, sandy beach, tidal pools, and deep-sea floor. The actinomorphic animals show different locomotive performance in different environment. Here, a series of experiments were conducted

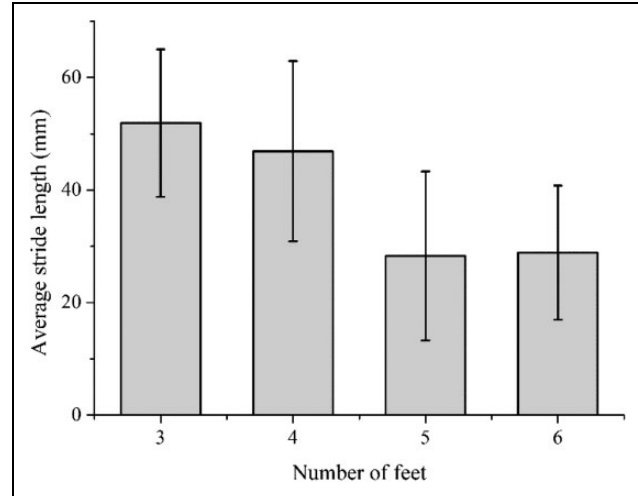


Figure 12. Average stride lengths of actinomorphic soft robots.

with the three-arm actinomorphic soft robot to analyze the locomotive performance under different circumstances.

In addition to moving in a flat terrestrial environment shown in previous experiments, the actinomorphic soft robot could move in a semisubmerged environment, as shown in Figure 13(a). The actinomorphic soft robot could achieve locomotion with an average stride length of 33 mm at a frequency of 1 Hz, as shown in Figure 13(b). In addition, the displacement of the actinomorphic soft robot exhibits a zig-zag trend at an average speed of 33 mm/s.

Sand is one ordinary intertidal zone habitat for actinomorphic animals, such as starfish. The three-arm actinomorphic soft robot could move on sand. Figure 14(a) shows a sequence of snapshots of locomotion on dry sand, and Figure 14(b) shows the displacement–time curve of the robot moving on dry sand at a frequency of 1 Hz. On dry sand, the soft robot could achieve locomotion with an average speed of 5.2 mm/s. Figure 15(a) shows a sequence of snapshots of locomotion on wet sand, and Figure 15(b) shows the displacement–time curve of the robot moving on wet sand at a frequency of 1 Hz. On wet sand, the soft robot could achieve locomotion with an average speed of 22.4 mm/s. These experimental results indicate that the performance for the actinomorphic soft robot moving with a zig-zag pattern on wet sand is superior to the performance for the actinomorphic soft robot moving on dry sand.

Transitional environment is one of the common terrains encountered in nature, for example, the water–land transitional zone. Figure 16(a) shows images from an experiment of a three-arm actinomorphic soft robot operating in a region transitioning from wet sand to a semisubmerged environment. Figure 16(b) shows the displacement–time curve for the forward translation from the wet sand environment to the semisubmerged environment. In this experiment, the soft robot moved at a frequency of 1 Hz. The soft robot could achieve locomotion with an average speed of

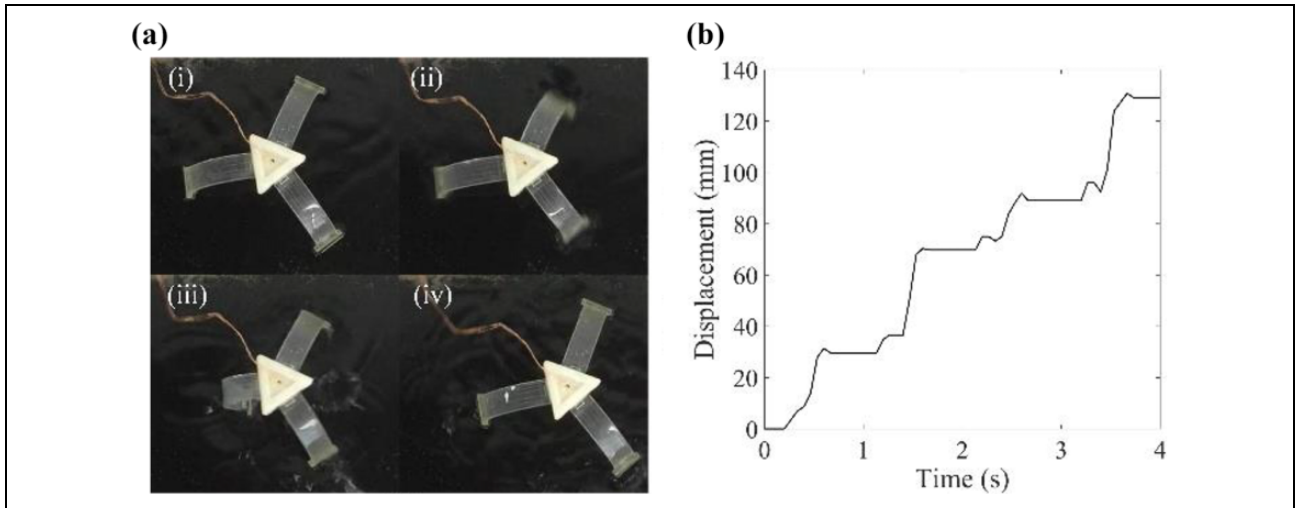


Figure 13. Locomotion in a semisubmerged environment. (a) Frames of locomotion in the semisubmerged environment. (b) Displacement–time curve for forward translation in the semisubmerged environment.

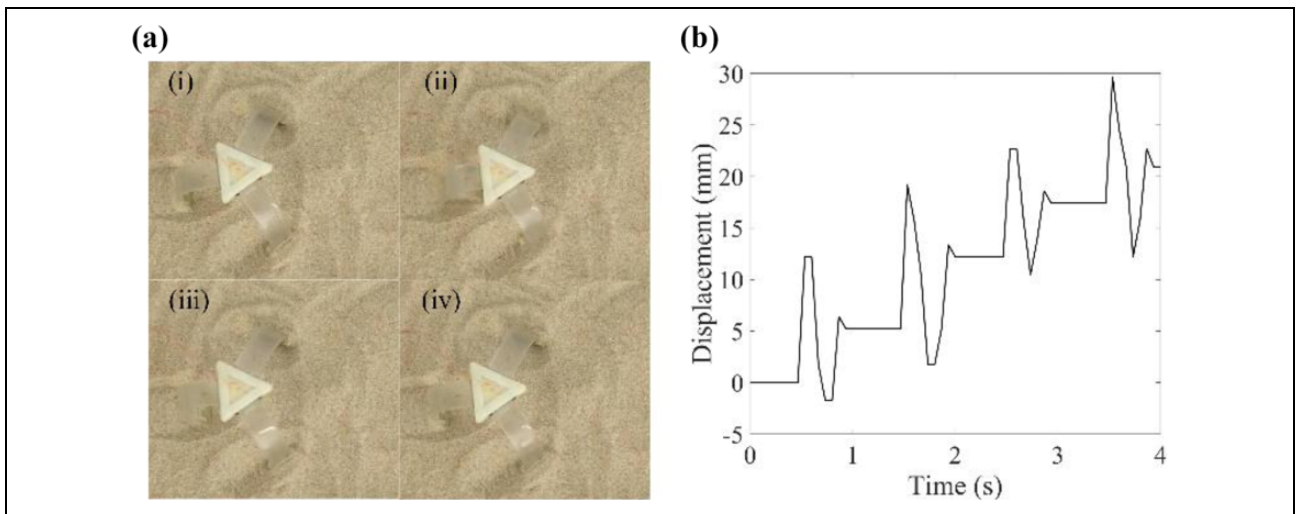


Figure 14. Locomotion on dry sand. (a) Frames of locomotion on dry sand. (b) Displacement–time curve for forward translation.

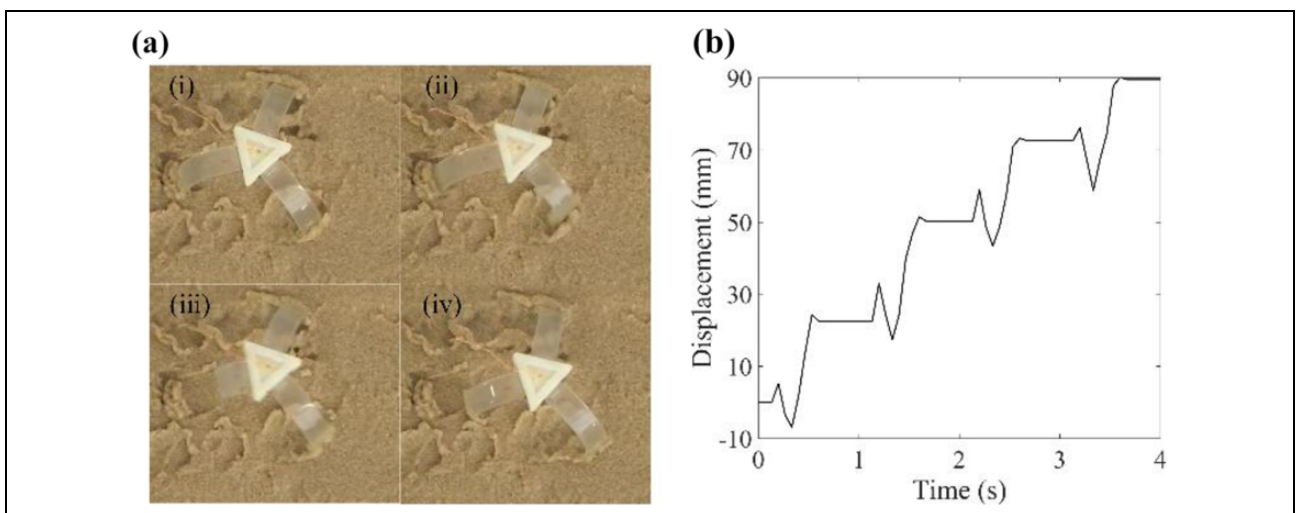


Figure 15. Locomotion on wet sand. (a) Frames of locomotion on wet sand. (b) Displacement–time curve for forward translation.

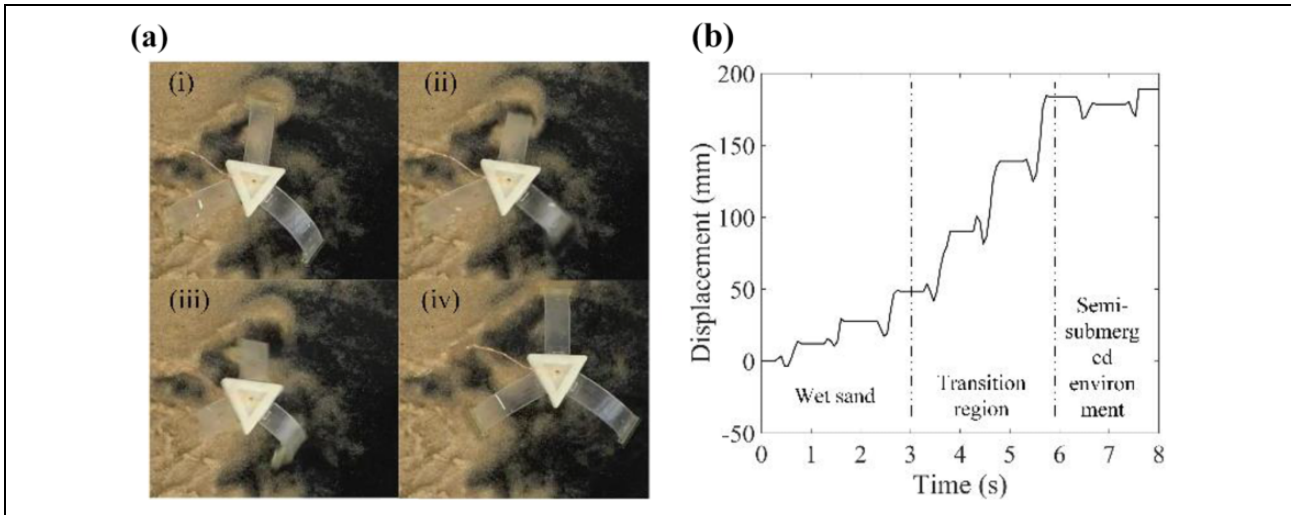


Figure 16. Moving from the wet sand to the semi-submerged environment. (a) Frames of locomotion in the environment. (b) Displacement–time curve for forward translation.

45 mm/s in the transition region and the performance in the transition region was superior to the performance in the other two surroundings.

Moving from the wet sand to the semisubmerged environment. (a) Frames of locomotion in the environment. (b) Displacement–time curve for forward translation.

Conclusion

A model was established to analyze the locomotion of the actinomorphic soft robot, combining the model of the soft arm with the spatial kinematics and the motion equation of the actinomorphic soft robot. Experimental and simulation results show that the actinomorphic soft robot moves on a flat surface with the zig-zag pattern caused by the switch of the locomotion state. Besides, the parameters of the wave gait for four actinomorphic soft robots with three to six arms were optimized according to the criterion of stride length. The three-arm actinomorphic soft robot outperforms other types of robots and could achieve a maximum stride length of 75 mm, which is nearly 0.4 times its body length. Moreover, the three-arm actinomorphic soft robot could achieve locomotion under different circumstances, including the semisubmerged environment, dry and wet sand as well as the transitional environment. Results show that the three-arm actinomorphic soft robot exhibits similar locomotion characteristic with the zig-zag movement pattern in various environment. Future work will focus on enhancing the autonomy and mobility of the actinomorphic soft robot.

Acknowledgement

The authors would like to thank Dr Hu Jin for his support and advice in writing this article.


Declaration of conflicting interests

The author(s) declared no potential conflicts of interest with respect to the research, authorship, and/or publication of this article.

Funding

The author(s) disclosed receipt of the following financial support for the research, authorship, and/or publication of this article: This work was supported by the National Natural Science Foundation of China (nos. 51105349 and 61375095).

ORCID iD

Gursel Alici  <http://orcid.org/0000-0001-6527-2881>

References

1. Rus D and Tolley MT. Design, fabrication and control of soft robots. *Nature* 2015; 521(7553): 467–475.
2. Pfeifer R, Lungarella M, and Iida F. The challenges ahead for bio-inspired ‘soft’ robotics. *Commun ACM* 2012; 55(11): 76–87.
3. Bauer S, Bauer-Gogonea S, Graz I, et al. 25th anniversary article: a soft future: from robots and sensor skin to energy harvesters. *Adv Mater* 2014; 26(1): 149–162.
4. Wehner M, Truby RL, Fitzgerald DJ, et al. An integrated design and fabrication strategy for entirely soft, autonomous robots. *Nature* 2016; 536(7617): 451–455.
5. Laschi C, Mazzolai B, and Cianchetti M. Soft robotics: technologies and systems pushing the boundaries of robot abilities. *Sci Robot* 2016; 1(1): eaah3690.
6. Mosadegh B, Polygerinos P, Keplinger C, et al. Pneumatic networks for soft robotics that actuate rapidly. *Adv Funct Mater* 2014; 24(15): 2163–2170.
7. Mutlu R, Alici G, and Li W. A soft mechatronic microstage mechanism based on electroactive polymer actuators. *IEEE ASME Trans Mech* 2016; 21(3): 1467–1478.
8. Nguyen CH, Alici G, and Mutlu R. A compliant translational mechanism based on dielectric elastomer actuators. *J Mech Des* 2014; 136(6): 061009.

9. Seok S, Onal CD, Cho KJ, et al. Meshworm: a peristaltic soft robot with antagonistic nickel titanium coil actuators. *IEEEASME Trans Mech* 2013; 18(5): 1485–1497.
10. Shepherd RF, Ilievski F, Choi W, et al. Multigait soft robot. *Proc Natl Acad Sci* 2011; 108(51): 20400–20403.
11. Shintake J, Rosset S, Schubert B, et al. Versatile soft grippers with intrinsic electroadhesion based on multifunctional polymer actuators. *Adv Mater* 2016; 28(2): 231–238.
12. Chen Z, Um TI, and Bart-Smith H. A novel fabrication of ionic polymer–metal composite membrane actuator capable of 3-dimensional kinematic motions. *Sens Actuat Phys* 2011; 168(1): 131–139.
13. Koh JS, Yang E, Jung GP, et al. Jumping on water: surface tension–dominated jumping of water striders and robotic insects. *Science* 2015; 349(6247): 517–521.
14. Jani JM, Leary M, Subic A, et al. A review of shape memory alloy research, applications and opportunities. *Mater Des* 2014; 56: 1078–1113.
15. Ma N, Song G, and Lee H. Position control of shape memory alloy actuators with internal electrical resistance feedback using neural networks. *Smart Mater Struct* 2004; 13: 777.
16. Lan CC, Lin CM, and Fan CH. A self-sensing microgripper module with wide handling ranges. *IEEEASME Trans Mech* 2011; 16(1): 141–150.
17. Wang TM, Shi ZY, Liu D, et al. An accurately controlled antagonistic shape memory alloy actuator with self-sensing. *Sensors* 2012; 12(6): 7682–7700.
18. Joseph SRD and Dhanalakshmi K. Shape memory alloy with bi-functionality in the master system to control a slave. *Sens Actuat Phys* 2016; 238: 351–360.
19. Wang G and Shahinpoor M. A new design for a rotatory joint actuator made with a shape memory alloy contractile wire. *J Intell Mater Syst Struct* 1997; 8: 215–219.
20. Dimitris CL. *Shape memory alloys: modeling and engineering applications*. New York: Springer, 2008.
21. Zhang S, Liu B, Wang L, et al. Design and implementation of a lightweight bioinspired pectoral fin driven by SMA. *IEEEASME Trans Mech* 2014; 19(6): 1773–1785.
22. Yuan H, Fauroux J, Chapelle F, et al. A review of rotary actuators based on shape memory alloys. *J Intell Mater Syst Struct* 2017; 28: 1863–1885.
23. Martinez RV, Glavan AC, Keplinger C, et al. Soft actuators and robots that are resistant to mechanical damage. *Adv Funct Mater* 2014; 24(20): 3003–3010.
24. Laschi C, Cianchetti M, Mazzolai B, et al. Soft robot arm inspired by the octopus. *Adv Robot* 2012; 26(7): 709–727.
25. Zhao H, O’Brien K, Li S, et al. Optoelectronically innervated soft prosthetic hand via stretchable optical waveguides. *Sci Robot* 2016; 1(1): eaai7529.
26. Tolley MT, Shepherd RF, Mosadegh B, et al. A resilient, untethered soft robot. *Soft Robot* 2014; 1(3): 213–223.
27. Lin HT, Leisk GG, and Trimmer B. GoQBot: a caterpillar-inspired soft-bodied rolling robot. *Bioinspir Biomim* 2011; 6(2): 026007.
28. Shepherd RF, Stokes AA, Freake J, et al. Using explosions to power a soft robot. *Angew Chem Int Ed* 2013; 52(10): 2892–2896.
29. Giorgio-Serchi F, Arienti A, Corucci F, et al. Hybrid parameter identification of a multi-modal underwater soft robot. *Bioinspir Biomim* 2017; 12(2): 025007.
30. Onal CD and Rus D. Autonomous undulatory serpentine locomotion utilizing body dynamics of a fluidic soft robot. *Bioinspir Biomim* 2013; 8(2): 026003.
31. Wang W, Lee JY, Rodrigue H, et al. Locomotion of inchworm-inspired robot made of smart soft composite (SSC). *Bioinspir Biomim* 2014; 9(4): 046006.
32. Song SH, Kim MS, Rodrigue H, et al. Turtle mimetic soft robot with two swimming gaits. *Bioinspir Biomim* 2016; 11(3): 036010.
33. Yu J, Xiao J, Li X, et al. Towards a miniature self-propelled jellyfish-like swimming robot. *Int J Adv Robot Syst* 2016; 13(5): 1729881416666796.
34. Mao S, Dong E, Jin H, et al. Gait study and pattern generation of a starfish-like soft robot with flexible rays actuated by SMAs. *J Bionic Eng* 2014; 11(3): 400–411.
35. Jin H, Dong E, Alici G, et al. A starfish robot based on soft and smart modular structure (SMS) actuated by SMA wires. *Bioinspir Biomim* 2016; 11(5): 056012.
36. Jin H, Dong E, Xu M, et al. Soft and smart modular structures actuated by shape memory alloy (SMA) wires as tentacles of soft robots. *Smart Mater Struct* 2016; 25(8): 085026.
37. Mohd JJ, Leary M, and Subic A. Designing shape memory alloy linear actuators: a review. *J Int Mater Syst Struct* 2017; 28(13): 1699–1718.
38. Mosley M, Mavroidis C, and Pfeiffer C. Design and dynamics of a shape memory alloy wire bundle actuator. In: *Proceedings of the ANS, 8th Topical Meeting on Robotics and Remote Systems*, Pittsburgh Pennsylvania, U.S.A, 25–29 April 1999, pp. 1–14. La Grange Park, IL: American Nuclear Society.
39. Rodrigue H, Wang W, Han MW, et al. An overview of shape memory alloy-coupled actuators and robots. *Soft Robot* 2017; 4(1): 3–15.
40. Wang G and Shahinpoor M. Design, prototyping and computer simulations of a novel large bending actuator made with a shape memory alloy contractile wire. *Smart Mater Struct* 1997; 6(2): 214–221.
41. Du Y, Liu B, Xu M, et al. Dynamic characteristics of planar bending actuator embedded with shape memory alloy. *Mechatronics* 2015; 25: 18–26.
42. Rodrigue H, Wang W, Kim DR, et al. Curved shape memory alloy-based soft actuators and application to soft gripper. *Compos Struct* 2017; 176: 398–406.
43. Liang C and Rogers CA. One-dimensional thermomechanical constitutive relations for shape memory materials. *J Int Mater Syst Struct* 1997; 8: 285–302.
44. Hannan MW and Walker ID. Kinematics and the implementation of an elephant’s trunk manipulator and other continuum style robots. *J Field Robot* 2003; 20(2): 45–63.
45. Jones BA and Walker ID. Kinematics for multisection continuum robots. *IEEE Trans Robot* 2006; 22(1): 43–55.

- 46. Umedachi T, Vikas V, and Trimmer B. Softworms: the design and control of non-pneumatic, 3D-printed, deformable robots. *Bioinspir Biomim* 2016; 11(2): 025001.
- 47. Cole LJ. Direction of locomotion of the starfish (*Asterias forbesi*). *J Exp Zool Part Ecol Genet Physiol* 1913; 14: 1–32.

Appendix I

Tables 1A to 1C show stride lengths in one period of different robots.

Table IA. Stride lengths (mm) of the three-arm actinomorphic robot in one period.

t_{11} (ms)				
λ_{12}	10	40	70	100
0.1	48	52	53	50
0.4	66	75	72	60
0.7	36	38	44	53
1.0	32	36	49	66

Table IB. Stride lengths (mm) of the four-arm actinomorphic robot in one period.^a

t_{21} (ms)					t_{21} (ms)				
λ_{22}	10	40	70	100	λ_{22}	10	40	70	100
0.1	53	46	46	52	0.1	46	50	51	48
0.4	54	50	53	52	0.4	40	52	53	53
0.7	NaN	NaN	NaN	NaN	0.7	22	20	40	37
1.0	NaN	NaN	NaN	NaN	1.0	21	23	64	58

(a) $\lambda_{23} = 0.1$

(b) $\lambda_{23} = 0.4$

t_{21} (ms)					t_{21} (ms)				
λ_{22}	10	40	70	100	λ_{22}	10	40	70	100
0.1	69	68	72	69	0.1	35	53	70	40
0.4	56	54	53	58	0.4	44	56	67	70
0.7	20	23	45	52	0.7	20	22	67	56
1.0	23	23	37	43	1.0	20	24	70	64

(c) $\lambda_{23} = 0.7$

(d) $\lambda_{23} = 1.0$

^aNaN indicates that it is difficult for the robot to move forward in a straight direction with these parameters.

Table IC. Stride lengths (mm) of the five-arm actinomorphic robot in one period.

t_{31} (ms)					t_{31} (ms)				
λ_{32}	10	40	70	100	λ_{32}	10	40	70	100
0.1	20	7	7	5	0.1	37	39	16	5
0.4	26	16	16	14	0.4	20	37	39	27
0.7	35	9	6	5	0.7	21	32	45	26
1.0	17	12	9	8	1.0	39	38	12	13

(a) $\lambda_{33} = 0.1$

(b) $\lambda_{33} = 0.4$

t_{31} (ms)					t_{31} (ms)				
λ_{32}	10	40	70	100	λ_{32}	10	40	70	100
0.1	40	46	47	42	0.1	35	43	42	25
0.4	23	27	54	44	0.4	41	44	63	35
0.7	24	21	62	57	0.7	40	45	40	23
1.0	15	17	24	29	1.0	39	26	20	20

(c) $\lambda_{33} = 0.7$

(d) $\lambda_{33} = 1.0$

Table ID. Stride lengths (mm) of the 6-arm actinomorphic robot in one period.

t_{41} (ms)					t_{41} (ms)				
λ_{42}	10	40	70	100	λ_{42}	10	40	70	100
0.1	27	23	20	21	0.1	20	47	48	52
0.4	30	26	44	43	0.4	28	31	39	35
0.7	20	24	23	21	0.7	22	35	25	15
1.0	17	18	19	15	1.0	16	22	22	17

(a) $\lambda_{44} = 0.1, \lambda_{43} = 0.1$

(b) $\lambda_{33} = 0.4$

t_{41} (ms)					t_{41} (ms)				
λ_{42}	10	40	70	100	λ_{42}	10	40	70	100
0.1	51	54	48	47	0.1	43	37	50	56
0.4	36	40	40	43	0.4	18	31	56	58
0.7	22	27	38	40	0.7	5	17	31	38
1.0	15	16	10	8	1.0	20	19	14	13

(c) $\lambda_{44} = 0.1, \lambda_{43} = 0.7$

(d) $\lambda_{44} = 0.1, \lambda_{43} = 1.0$

t_{41} (ms)					t_{41} (ms)				
λ_{42}	10	40	70	100	λ_{42}	10	40	70	100
0.1	11	23	15	10	0.1	27	39	44	32
0.4	22	32	29	26	0.4	38	37	35	28
0.7	32	25	28	28	0.7	32	35	28	34
1.0	10	13	10	7	1.0	10	22	12	15

(e) $\lambda_{44} = 0.4, \lambda_{43} = 0.1$

(f) $\lambda_{44} = 0.4, \lambda_{43} = 0.4$

t_{41} (ms)					t_{41} (ms)				
λ_{42}	10	40	70	100	λ_{42}	10	40	70	100
0.1	25	51	56	42	0.1	35	37	53	50
0.4	38	42	42	41	0.4	22	32	41	48
0.7	23	34	30	35	0.7	11	23	42	45
1.0	10	14	10	15	1.0	10	8	16	18

(g) $\lambda_{44} = 0.4, \lambda_{43} = 0.7$

(h) $\lambda_{44} = 0.4, \lambda_{43} = 1.0$

t_{41} (ms)					t_{41} (ms)				
λ_{42}	10	40	70	100	λ_{42}	10	40	70	100
0.1	17	22	20	15	0.1	15	39	30	21
0.4	16	40	47	45	0.4	26	45	43	31
0.7	21	27	41	48	0.7	31	25	21	25
1.0	18	25	10	12	1.0	25	29	24	17

(i) $\lambda_{44} = 0.7, \lambda_{43} = 0.1$

(j) $\lambda_{44} = 0.7, \lambda_{43} = 0.4$

t_{41} (ms)					t_{41} (ms)				
λ_{42}	10	40	70	100	λ_{42}	10	40	70	100
0.1	18	26	23	21	0.1	14	26	25	27
0.4	15	37	30	32	0.4	21	43	42	46
0.7	17	22	24	24	0.7	21	41	40	33
1.0	14	17	16	12	1.0	15	32	36	38

(k) $\lambda_{44} = 0.7, \lambda_{43} = 0.7$

(l) $\lambda_{44} = 0.7, \lambda_{43} = 1.0$

t_{41} (ms)					t_{41} (ms)				
λ_{42}	10	40	70	100	λ_{42}	10	40	70	100
0.1	25	13	10	11	0.1	31	36	15	20
0.4	22	15	17	16	0.4	31	41	40	34
0.7	23	30	33	30	0.7	38	56	47	44
1.0	25	17	16	13	1.0	33	29	21	17

(m) $\lambda_{44} = 1.0, \lambda_{43} = 0.1$

(n) $\lambda_{44} = 1.0, \lambda_{43} = 0.4$

t_{41} (ms)					t_{41} (ms)				
λ_{42}	10	40	70	100	λ_{42}	10	40	70	100
0.1	41	40	39	41	0.1	34	31	33	27
0.4	39	40	49	46	0.4	36	36	43	38
0.7	25	28	27	32	0.7	34	37	36	43
1.0	36	37	35	32	1.0	35	34	27	24

(o) $\lambda_{44} = 1.0, \lambda_{43} = 0.7$

(p) $\lambda_{44} = 1.0, \lambda_{43} = 1.0$